Empirical Dust Attenuation Models: Taking Hydrodynamical Simulatons with a Grain of Dust

ChangHoon Hahn,[1, *] Tjitske K. Starkenburg,[2] and IQ Collaboratory

[1]*Department of Astrophysical Sciences, Princeton University, Peyton Hall, Princeton NJ 08544, USA*
[2]*Center for Interdisciplinary Exploration and Research in Astrophysics (CIERA) and Department of Physics and Astronomy, 1800 Sherman Ave, Evanston IL 60201, USA*

(Dated: `DRAFT -- cff9046 -- 2020-12-10 -- NOT READY FOR DISTRIBUTION`)

ABSTRACT

We present the Empirical Dust Attenuation (EDA) model, an empirical framework for applying dust attenuation to simulated galaxy populations. The EDA uses an observationally motivated parametrization of attenuation and a statistical prescription for assigning the curves that includes correlations with galaxy properties. We apply the EDA separately to three state-of-the-art hydrodynamical simulations (SIMBA, IllustrisTNG, and EAGLE) and forward model their optical and UV color-magnitude relations, $(g-r)-M_r$ and $(FUV-NUV)-M_r$. We then compare them to a volume-limited galaxy sample from SDSS and GALEX observations using simulation-based inference. With the EDA, we accurately reproduce the color magnitude relations of the observational sample for TNG and EAGLE. For SIMBA, we struggle to reproduce observations due to an overprediction of starburst galaxies. The bestfit EDA s for TNG and EAGLE also predict attenuation–slope relations and attenuation curves of star-forming galaxies in good agreement with observations. Beyond reproducing observations, the EDA also sheds light on dust attenuation in quiescent galaxies, which is challenging to measure observationally. We find that quiescent galaxies have significant UV and optical attenuation but with shallow slopes, in contrast to star-forming galaxies. For the entire galaxy population, we find that more massive galaxies require higher overall dust attenuation while galaxies with higher specific star formation rates have steeper attenuation curves. In addition to improving our understanding of dust in galaxies, our results underscore the advantages of the EDA and the forward modeling approach.

Keywords: keyword1 – keyword2 – keyword3

1. INTRODUCTION

Dust in the interstellar medium of a galaxy can dramatically impact the observed light from the galaxy over the full range of the electromagnetic spectrum. It emits in the infrared (IR) and

---

* hahn.changhoon@gmail.com

modifies the galaxy's stellar radiation through absorption and scatter from the near-infrared (NIR) to ultraviolet (UV). Dust can, therefore, dramatically impact the physical properties of galaxies we infer from optical and UV light, such as star formation rate (SFR), stellar mass (M_*), or stellar ages (see reviews by Walcher et al. 2011; Conroy 2013). Since these properties are the building blocks for our understanding of galaxies and how they evolve, a better understanding of dust no only provides insights into the physical processes related to dust, but it also underpins all galaxy studies.

The combined effect of dust on the spectral energy distribution (SED) of a galaxy is typically described using an attenuation curve, $A(\lambda)$. Observations have now established the major features in $A(\lambda)$. In the UV, the curve steeply rises due to absorptions by small grains. At 2175, in the near-UV (NUV), there is absorption bump referred to as the "UV dust bump". At longer wavelengths, the curves on take a power-law shape. For an overview, we refer to reviews by Calzetti (2001); Draine (2003); Galliano et al. (2018). Attenuation curves, however, are not universal. Observations find a wide range of attenuation curves in the local Universe (Wild et al. 2011; Battisti et al. 2017; Salim et al. 2018; Salim & Narayanan 2020) as well as at high redshifts (*e.g.* Reddy et al. 2015; Salmon et al. 2016).

To understand the origin of this variation in attenuation curves, a number of observational works have examined the correlation between dust attenuation and galaxy properties. Using 23,000 star-forming galaxies in the Sloan Digital Sky Survey (SDSS), Wild et al. (2011) found that the slope of the attenuation curves varies strongly with galaxy axial ratio and weakly with specific SFR (SSFR). Similarly, Battisti et al. (2017), from 5,500 star-forming galaxies, found tentative trends with stellar age, specific star formation rate, stellar mass, and metallicity. Meanwhile, Salim et al. (2018), from 230,000 galaxies in the GALEX-SDSS-WISE Legacy Catalog 2 (GSWLC2), find a significant M_* dependence on the slope. They argue that this is caused by the underlying "attenuation-slope relation", a trend between the amplitude of the V-band attenuation (A_V) and slope, where galaxies with higher A_V have shallower slopes. At low attenuation, dust scattering dominates absorption so the attenuation curve steepens because red light scatters isotropically while blue light scatters forward (Gordon et al. 1994; Witt & Gordon 2000; Draine 2003). At high attenuation dust absorption is dominant and the attenuation curve is shallower (Chevallard et al. 2013). Nevertheless, there is still no clear consensus on the connection between attenuation curves and galaxy properties. Also, studies so far have focused on star-forming galaxies and little is known about dust attenuation in quiescent galaxies.

Alongside observations, theoretical efforts that model radiative transfer of stellar light through a dusty ISM also provide insights into dust attenuation. Radiative transfer models span a wide range of geometric configurations of stars and dust. For instance, models focused on isolating the physical effects of dust have considered simple slab or shell-like dust geometries illuminated by stellar radiation (*e.g.* Witt & Gordon 1996, 2000; Seon & Draine 2016). Other models, focused on modeling dust attenuation in galaxies as a whole, have applied 3D dust radiative transfer in hydrodynamic simulations of idealized galaxies (*e.g.* Jonsson 2006; Rocha et al. 2008; Hayward & Smith 2015; Natale et al. 2015; Hou et al. 2017). Dust attenuation has also been examined in a cosmological context using semi-analytic models (SAMs) that do not track baryonic growth directly but make simple physically motivated assumptions about the resulting galaxy properties from dark matter growth (*e.g.* Granato

et al. 2000; Fontanot et al. 2009; Wilkins et al. 2012; Gonzalez-Perez et al. 2013). Lastly, radiative transfer models have recently been applied to cosmological hydrodynamical simulations (*e.g.* Camps & Baes 2015; Narayanan et al. 2018; Trayford et al. 2020). As in observations, simulations find significant variation in attenuation curves.

Despite their progress, there are still major challenges for radiative transfer models. For instance, they produce attenuation-slope relations that are significantly steeper than observations. Many models also require significant hand-tuning (*e.g.* propagating rays/photons into particular cells). Assumptions in the underlying dust grain models also produce systematic uncertainties that are difficult to quanitfy (see Steinacker et al. 2013, for a review). Lastly, radiative transfer models are computationally expensive. Applying a range of radiative transfer dust models to multiple simulations for comparisons is prohibitive. Using Markov Chain Monte Carlo sampling with them for parameter exploration or to marginalize over the impact of dust would be *intractable*.

In this paper, we take a different approach and present the Empirical Dust Attenuation (EDA) model, a flexible framework for statistically applying dust attenuation to galaxy populations. The EDA model assigns, to every galaxy, a different dust attenuation curve. The attenuation curves are parameterized with a functional-form used in observational studies (Noll et al. 2009) and the parameters of the curve for each galaxy (*e.g.* optical depth, slope) is sampled from distributions set by the EDA model parameters and the galaxy's properties. By sampling the attenuation curve parameters, it produces realistic variations among the attenuation curves. The EDA does not seek to produce realistic dust attenuation for individual galaxies, like radiative transfer models. Instead, it aims to produce realistic dust attenuations for the entire galaxy sample and enable galaxy population-to-population comparisons.

There are a number of advantages to our EDA approach. The EDA uses the same functional-form for the attenuation curves as observational studies, so predictions of the model can easily be compared to observational constraints. We also formulate the EDA parameters so that they are easily interpretable and directly reveal correlations between dust attenuation and galaxy properties. Lastly, the EDA model is computationally inexpensive.

The EDA model, with its flexibility and speed, provides a crucial step in a *forward modeling approach* to comparing simulations to observations (*e.g.* Nelson et al. 2018; Baes et al. 2019; Trčka et al. 2020; Dickey et al. 2020). In the standadrd approach, the galaxy properties (*e.g.* SFR, M_*) predicted by simulations are compared to those derived from observations. In the forward modeling approach, observables (*e.g.* magnitude, color) are *forward modeled* for each galaxy in the simulations; then the simulations are compared to observations in observational space. With a forward modeling approach, comparisons are not limited by variations, inconsistencies, and biases of different observational methods for measuring galaxy properties (*e.g.* different tracers of SFR or M_*). Selection functions and systematic effects can also be accounted for in the forward model.

Of course, to produce realistic observables of simulated galaxies, the forward model must include some prescription for applying dust attenuation. In principle, a radiative transfer model can be used for this purpose; however, its computational cost would severely limit any exploration of the "dust parameters". With the EDA, however, we can apply a wide range of realistic dust attenuation to

Figure 1. The stellar mass functions, Φ_{M_*} (left-most panel), and $M_* - $SFR relation (right panels) of galaxies in three cosmological hydrodynamic simulations: SIMBA (orange), TNG (blue), and EAGLE (green). For reference, we include Φ_{M_*} (black) and the $M_* - $SFR relation (black dashed) of our observational sample from SDSS. Uncertainties for the SDSS Φ_{M_*} are derived using jackknife resampling. We describe the simulations and observations above in Section 2. *Differences in Φ_{M_*} and the $M_* - $SFR relations among the hydrodynamic simulations highlight how they predict galaxy populations with significantly different the physical properties.*

simulated galaxies in a matter of seconds and easily explore and sample the EDA parameter space to infer the relationship between dust attenuation and galaxy properties. *For readers uninterested in dust*, the EDA provides a way to treat dust parameters as *nuisance* parameters and tractably marginalize over dust attenuation.

In this work, we present a simple EDA model that uses the Noll et al. (2009) attenuation curve parameterization and includes correlations between dust attenuation and galaxy M_* and SFR (Section 3). We apply the EDA separately to three state-of-the-art cosmological large-scale hydrodynamical simulations (SIMBA, IllustrisTNG, and EAGLE), which we describe in Section 2, and compare them to a volume-limited galaxy sample from SDSS and GALEX observations (Section 2.4). In Section 3, we describe our EDA model in detail. Finally, in Section 5, we present the results of our comparison and discuss their implications for our understanding of dust attenuation as well as of its connection to galaxy properties.

2. DATA

In this paper, we present the Empirical Dust Attenuation (EDA) model and demonstrate how it can be used in a forward modeling approach to compare galaxy populations in simulations and observations. For our simulations, we use three cosmological hydrodynamical simulations: the Illustris TNG (hereafter TNG), EAGLE, and SIMBA. For our observations, we use a galaxy sample derived from SDSS. Below, we briefly describe the hydrodynamical simulations and the SDSS observations used throughout this work.

In Figure 1, we present the stellar mass functions, Φ_{M_*} left-most panel, and $M_* - $SFR relations (right panels) of galaxies in the SIMBA (orange), TNG (blue), and EAGLE (green) cosmological hydrodynamic simulations. For reference, we include Φ_{M_*} and the $M_* - $SFR relation for our observational SDSS galaxy sample. For the simulations, M_* is the total stellar mass within the host

halo, excluding any stellar mass in subhalos; SFR is the instantaneous SFR derived from dense and cold gas. For SDSS, M_* is estimated using `kcorrect` (Blanton & Roweis 2007) assuming a Chabrier (2003) initial mass function and SFR is from the current release of Brinchmann et al. (2004)[1]. The uncertainties for the SDSS SMF are derived from jackknife resampling. Figure 1 illustrates that the hydrodynamical simulations predict significantly different SMFs and $M_* -$ SFR relations. This difference, which was also recently highlighted in Hahn et al. (2019c), demonstrates that *the hydrodynamical simulations predict galaxy populations with significantly different physical properties*.

2.1. *Illustris TNG*

The Illustris TNG simulation[2] is a cosmological hydrodynamic simulation of comoving volume $(110.7\,\mathrm{Mpc})^3$ (Nelson et al. 2018; Pillepich et al. 2018; Springel et al. 2018). It improves on the original Illustris simulation[3] (Vogelsberger et al. 2014; Genel et al. 2014; public data release by Nelson et al. 2015), by including magneto-hydrodynamics and updated treatments for galactic winds, metal enrichment, and AGN feedback. Most notably, TNG uses a new implementation for feedback from SMBH (Weinberger et al. 2018), where feedback energy is injected in the form of a kinetic AGN-driven wind at low SMBH accretion rates. This new implementation has been shown to alleviate discrepancies found between the original Illustris and observations for $> 10^{13-14} M_\odot$ massive halos.

2.2. *EAGLE*

The Virgo Consortium's EAGLE project[4] (Schaye et al. 2015; Crain et al. 2015; McAlpine et al. 2016) is a publicly available suite of cosmological hydrodynamic simulations constructed using An-archy (Dalla Vecchia et al. in prep.; see also Appendix A of Schaye et al. 2015), a modified version of the GADGET-3 code (Springel 2005). We use the L0100Ref simulation, which has a comoving volume of $(100\,\mathrm{Mpc})^3$. EAGLE has subgrid models for star formation, stellar mass loss, metal enrichment and stellar feedback that stochastically inject thermal energy in the ISM as in (Dalla Vecchia & Schaye 2012). The feedback energy from AGN is also added to surrounding gas stochastically (Booth & Schaye 2009). Parameters of the stellar feedback and SMBH accretion are calibrated to broadly reproduce the $z = 0$ stellar mass function and galaxy stellar size-stellar mass relation. Meanwhile, the AGN feedback efficiency is calibrated to match the SMBH-galaxy mass relation.

2.3. *SIMBA*

The Simba simulation suite (Davé et al. 2019), the successor to Mufasa (Davé et al. 2016, 2017a,b), is a cosmological hydrodynamical simulation construted using Gizmo, a meshless finite mass hydrodynamics code (Hopkins 2015; Hopkins et al. 2017). Of the simulations, we use 'm100n1024', which has a box size of $(100\,h^{-1}\,\mathrm{Mpc})^3$ and baryonic mass resolution of $1.82 \times 10^7\ M_\odot$. The simulation uses the same subgrid models as Mufasa for H_2 based star formation, decoupled two-phase winds for star formation driven galactic winds, and feedback from Type I supernovae and AGB stars. Meanwhile, it uses updated models for AGN feedback and on-the-fly dust model. Simba

---

[1] http://www.mpa-garching.mpg.de/SDSS/DR7/
[2] https://www.tng-project.org/
[3] http://www.illustris-project.org
[4] http://www.eaglesim.org

uses a two-mode SMBH accretion model, torque-limited accretion for cold gas (Anglés-Alcázar et al. 2017) and Bondi-based accretion for hot gas, and two-mode AGN feedback.

2.4. *SDSS Galaxies*

For our observations, we use a galaxy sample derived from SDSS observations. We start with the $M_* > 10^{9.4}h^{-2}M_\odot$ complete Tinker et al. (2011) volume-limited sample and then impose a $M_r < -20$ completeness cut. The original Tinker et al. (2011) sample is derived from the SDSS DR7 (Abazajian et al. 2009) NYU Value-Added Galaxy Catalog (VAGC; Blanton et al. 2005). In this work, we focus on observables that can be consistently defined and derived in both simulations and observables: the r-band absolute magnitude, M_r, the optical $g-r$ color, and the $FUV-NUV$ color. For the SDSS sample, we use FUV, NUV, r and g band absolute magnitudes from the NASA-Sloan Atlas[5], which is re-reduction of SDSS DR8 (Aihara et al. 2011) that includes an improved background subtraction (Blanton et al. 2011) and near and far UV photometry from GALEX. These absolute magnitudes are derived using `kcorrect` (Blanton & Roweis 2007), assuming a Chabrier (2003) initial mass function.

2.5. *Forward Modeling Observations*

One of the main goals of this work is to conduct an "apples-to-apples" comparison between the simulations and observations using a forward modeling approach. A crucial step is to forward model the observables for our simulations — in this work, we use r-band luminosity (M_r), optical color ($g-r$), and UV color ($FUV-NUV$). As the first step, we construct SEDs for all of the simulated galaxies based on their star formation and metallicity histories (SFH and ZH) using the Fleixble Stellar Population Synthesis model (`FSPS`; Conroy et al. 2009, 2010).

For each simulated galaxy, we bin the total stellar mass formed by age (t) and metallicity (Z). We use a consistent t, Z grid for all of the simulations to account for the variable time and mass resolutions. For each point in the t, Z grid, we generate the spectrum of a simple stellar population (SSP) using `FSPS` and take the linear combination of them, weighted by the total stellar mass formed in the bin, to produce the galaxy SED. We use a Chabrier (2003) initial mass function. For further details on how we construct the SEDs, we refer readers to Starkenberg et al. (in prep.).

Next in the forward model, we use the EDA model to assign dust attenuation curves for each of simulated galaxy based on its physical properties and apply dust attenuation to its SEDs. We describe the EDA in detail in Section 3. From the dust attenuated SEDs, we measure the observables by convolving them with transmission curves of the GALEX FUV, GALEX NUV, SDSS g, and SDSS r broadband filters. Lastly, we add realistic noise to M_r, $g-r$, and $FUV-NUV$ by sampling from the observed uncertainty distributions of the NASA Sloan-Atlas.

In Figure 2 we present the forward modeled optical and UV color-magnitude relations, $(g-r)-M_r$ (top) and $(FUV-NUV)-M_r$ (bottom), for simulated galaxies of SIMBA (left), TNG (center) and EAGLE (right). The observables for the simulations do not yet include any prescription for dust attenuation. Comparison to SDSS observations (black dashed) clearly demonstrate that *without*
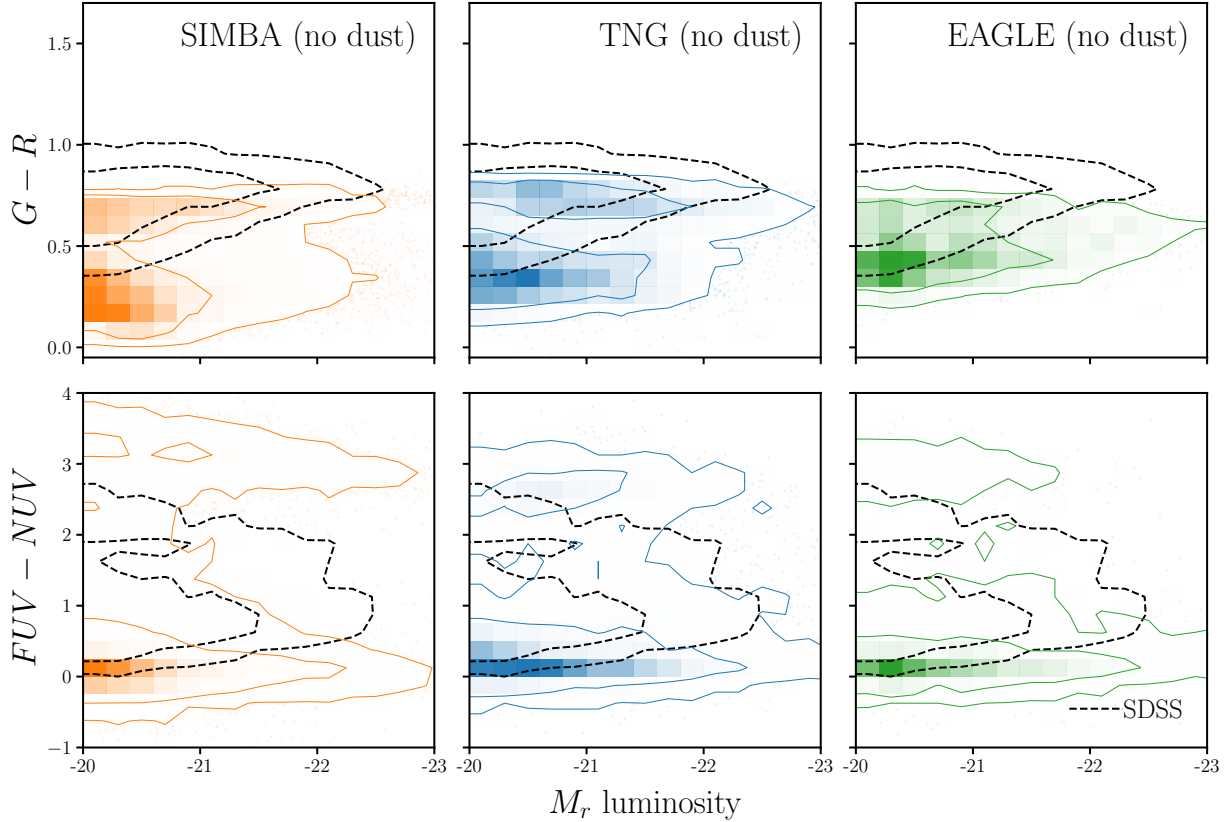
---

[5] http://nsatlas.org/

Figure 2. We present the forward modeled optical and UV color-magnitude relations of simulated galaxies in SIMBA (left), TNG (center), and EAGLE (right). The simulations above do *not* yet include any prescription for dust attenuation. $(g-r) - M_r$ (top) and $(FUV-NUV) - M_r$ (bottom) are the main observables used throughout the paper. They are derived using SEDs constructed from the star-formation and metallicity of the simulated galaxies. These observables are consistently defined and measured as our SDSS sample (Section 2.5), which we include for comparison (black dashed). *Without dust, the hydrodynamical simulations cannot reproduce the observed optical or UV color-magnitude.*

dust attenuation, the hydrodynamical simulations cannot reproduce the observed optical or UV color-magnitude relations.

3. THE EMPIRICAL DUST ATTENUATION MODEL

In this section we describe the Empirical Dust Attenuation (EDA) model, a flexible prescription for applying dust attenuation curves to galaxy populations. With the EDA, we can apply a wide variety of dust attenuation and include correlation between dust attenuation and physical galaxy properties. Later, we demonstrate that we can accurately reproduce SDSS observations with the EDA and use it to test galaxy formation models and shed light on dust in galaxies.

We define the dust attenuation curve, $A(\lambda)$, as

$$F_o(\lambda) = F_i(\lambda)10^{-0.4A(\lambda)} \tag{1}$$

where F_o is the observed flux and F_i is the intrinsic flux. We normalize the attenuation at the V band,

$$A(\lambda) = A_V \frac{k(\lambda)}{k_V} \tag{2}$$

so that A_V determines the amplitude of the attenuation, while $k(\lambda)$ determines the wavelength dependence.

To determine $A(\lambda)$ for each galaxy, we first assign A_V using the slab model from (*e.g.* Somerville & Primack 1999; Somerville et al. 2012) where A_V is calculated based on the inclination of the galaxy, i, and its optical depth, τ_V:

$$A_V = -2.5 \log \left[\frac{1 - e^{-\tau_V \sec i}}{\tau_V \sec i} \right]. \tag{3}$$

For each galaxy, we uniformly sample i from 0 to $\pi/2$. Then in τ_V we include the correlation between A_V and galaxy properties (M_* and SSFR), found in both observations and simulations (*e.g.* Narayanan et al. 2018; Salim & Narayanan 2020). We parameterize τ_V with a simple and linear M_* and SSFR dependence:

$$\tau_V(M_*, \mathrm{SFR}) = m_{\tau, M_*} \log \left(\frac{M_*}{10^{10} M_\odot} \right) + m_{\tau, \mathrm{SSFR}} \log \left(\frac{\mathrm{SSFR}}{10^{-10} yr^{-1}} \right) + c_\tau. \tag{4}$$

m_{τ, M_*}, $m_{\tau, \mathrm{SSFR}}$, and c_τ represent the M_* dependence, the SSFR dependence, and overall amplitude of τ_V. Since τ_V is optical depth, we impose a $\tau_V \geq 0$ limit.

The slab model is a naive approximation. In reality, A_V for a galaxy depends on complexities of its star-to-dust geometry, variations in the extinction curves, and other properties beyond just inclination and τ_V. The purpose of the EDA, however, is not to accurately model dust attenuation for individual galaxies, but rather to accurately represent the distribution of dust attenuation for galaxy populations. In this regard, the slab model is consistent with the correlation between A_V and i found in the literature: edge-on galaxies have higher A_V than face-on galaxies (*e.g.* Conroy et al. 2010; Wild et al. 2011; Battisti et al. 2017; Salim & Narayanan 2020). More importantly, the A_V distribution, $p(A_V)$, produced using the slab model with uniformly sampled inclinations closely matches the $p(A_V)$ of our SDSS sample (Figure 10). Also, replacing the slab model with a more flexible prescription for sampling A_V does not significant impact our analysis (Appendix B). Therefore, we conclude that the slab model is a sufficient, flexible empirical prescription for sampling A_V.

For the wavelength dependence of the attenuation curve, $k(\lambda)$, we use the Noll et al. (2009) parameterization:

$$k(\lambda) = (k_{\mathrm{Cal}}(\lambda) + D(\lambda)) \left(\frac{\lambda}{\lambda_V} \right)^\delta. \tag{5}$$

Here $k_{\mathrm{Cal}}(\lambda)$ is the Calzetti (2001) curve:

$$k_{\mathrm{Cal}}(\lambda) = \begin{cases} 2.659(-1.857 + 1.040/\lambda) + R_V, & 6300A \leq \lambda \leq 22000A \\ 2.659(-2.156 + 1.509/\lambda - 0.198/\lambda^2 + 0.011/\lambda^3) + R_V & 1200A \leq \lambda \leq 6300A \end{cases}$$

where $\lambda_V = 5500A$ is the V band wavelength and δ is the slope offset of the attenuation curve from k_{Cal}. Since δ correlates with galaxy properties (*e.g.* Leja et al. 2017; Salim et al. 2018), we

parameterize δ with a similar M_* and SSFR dependence as τ_V:

$$\delta(M_*, \text{SFR}) = m_{\delta,M_*} \log\left(\frac{M_*}{10^{10}M_\odot}\right) + m_{\delta,\text{SFR}} \log\left(\frac{\text{SSFR}}{10^{-10}yr^{-1}}\right) + c_\delta. \tag{6}$$

$D(\lambda)$ in Eq. 5 is the UV dust bump, which we parameter using the standard Lorentzian-like Drude profile:

$$D(\lambda) = \frac{E_b(\lambda\,\Delta\lambda)^2}{(\lambda^2 - \lambda_0^2)^2 + (\lambda\,\Delta\lambda)^2} \tag{7}$$

where λ_0, $\Delta\lambda$, and E_b are the central wavelength, FWHM, and strength of the bump, respectively. We assume fixed $\lambda_0 = 2175A$ and $\Delta\lambda = 350A$. Kriek & Conroy (2013) and Tress et al. (2018) find that E_b correlates with the δ for star-forming galaxies $z \sim 2$. Narayanan et al. (2018) confirmed this dependence in simulations. For the EDA model, we assume a fixed relation between E_B and δ from Kriek & Conroy (2013): $E_b = -1.9\,\delta + 0.85$. Allowing the slope and amplitude of the E_B and δ relation to vary does *not* impact our results; however, we do not derive any meaningful constraints on them either. In Table 1, we list and describe all of the free parameters in the EDA.

SSFR of galaxies are used to calculate τ_V and δ in Eqs. 4 and 6. However, due to mass and temporal resolutions, some galaxies in the simulations have SFR $= 0$ — *i.e.* an unmeasurably low SFR (Hahn et al. 2019c). They account for 17, 19, 9% of galaxies in SIMBA, TNG, and EAGLE, respectively. Since Eqs. 4 and 6 depend on log SSFR, they cannot be used in the equations to derive τ_V and δ for these galaxies. To account for this issue, we assign $\text{SFR}_{\min}$, the minimum non-zero SFR in the simulations, to SFR $= 0$ galaxies when calculating τ_V and δ. For SIMBA, TNG, and EAGLE, $\text{SFR}_{\min} = 0.000816$, 0.000268, and $0.000707 M_\odot/yr$. Although this assumes that SFR $= 0$ galaxies have similar dust properties as the galaxies with SFR $= \text{SFR}_{\min}$, since the simulations have very low $\text{SFR}_{\min}$ we expect galaxies with SFR $= \text{SFR}_{\min}$ to have little recent star-formation and low gas mass, similar to SFR $= 0$ galaxies.

In practice, to apply the EDA to a simulated galaxy population, we begin by assigning a uniformly sample inclination, i, to each galaxy. Then τ_V, and δ are calculated for the galaxy based on its i, M_*, SSFR and the EDA parameters. From τ_V and δ, we determine A_V and $k(\lambda)$, which together gives $A(\lambda)$. Afterwards, we attenuate the galaxy SEDs using Eq. 1 and use the attenuated SEDs to calculate the observables: G, R, NUV, and FUV absolute magnitudes. In Figure 3, we present attenuation curves, $A(\lambda)$, generated by the EDA for galaxies with different SFR and M_*: star-forming (SFR $= 10^{0.5} M_\odot/yr$) with low mass ($10^{10} M_\odot$; blue), with high mass ($10^{11} M_\odot$; green) and quiescent (SFR $= 10^{-2} M_\odot/yr$) with low mass ($10^{10} M_\odot$; orange), with high mass ($10^{11} M_\odot$; red). All galaxies are edge-on (*i.e.* $i = 0$) and we use EDA parameters: $\{m_{\tau,M_*}, m_{\tau,\text{SSFR}}, c_\tau, m_{\delta,M_*}, m_{\delta,\text{SFR}}, c_\delta\} = \{2., -2., 2., -0.1, -0.1, -0.2\}$, arbitrarily chosen within the prior range listed in Table 1. For comparison, we include the Calzetti (2001) attenuation curve. Even for only edge-on galaxies, the EDA produces attenuation curves with a wide range of amplitude and slope to galaxies based on their physical properties.

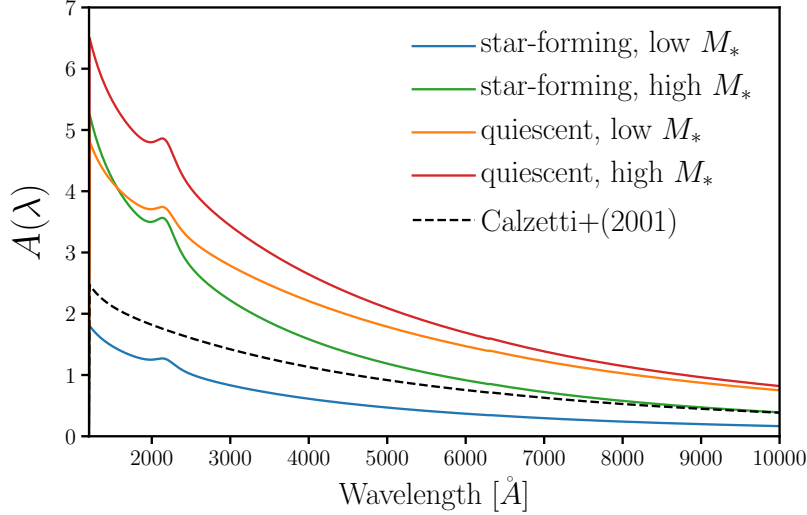## 4. SIMULATION-BASED INFERENCE: APPROXIMATE BAYESIAN COMPUTATION

Figure 3. Attenuation curves, $A(\lambda)$, generated by the Empircial Dust Attenuation (EDA) model for galaxies with different SFR and M_*. We include $A(\lambda)$ for star-forming (SFR $= 10^{0.5} M_\odot/yr$) low mass galaxy ($10^{10} M_\odot$; blue), high mass galaxy ($10^{11} M_\odot$; green) and quiescent (SFR $= 10^{-2} M_\odot/yr$) low mass galaxy ($10^{10} M_\odot$; orange), high mass galaxy ($10^{11} M_\odot$; red). All galaxies are edge-on (*i.e.* $i = 0$) and we use EDA parameter values near the center of our prior range: $\{m_{\tau,M_*}, m_{\tau,\mathrm{SSFR}}, c_\tau, m_{\delta,M_*}, m_{\delta,\mathrm{SFR}}, c_\delta\} = \{2., -2., 2., -0.1, -0.1, -0.2\}$ (Table 1). For comparison, we include the Calzetti (2001) attenuation curve. In the EDA, the amplitude and slope of $A(\lambda)$ depend on M_*, and SSFR (Eqs. 4 and 6). *The EDA provides a flexible model for applying dust attenuation to galaxies based on their physical properties.*

Table 1. Free parameters of the Empirical Dust Attenuation Model

Parameter	Definition	prior
m_{τ,M_*}	M_* dependence of the optical depth, τ_V	flat $[-5., 5.]$
$m_{\tau,\mathrm{SSFR}}$	SSFR dependence of τ_V	flat $[-5., 5.]$
c_τ	amplitude of τ_V	flat $[0., 6.]$
m_{δ,M_*}	M_* dependence of δ, the attenuation curve slope offset	flat $[-4., 4.]$
$m_{\delta,\mathrm{SFR}}$	SSFR dependence of δ	flat $[-4., 4.]$
c_δ	amplitude of δ	flat $[-4., 4.]$

With a forward modeling approach and the EDA model, we can generate observables for simulated galaxies and make an "apples-to-apples" compraison to SDSS observations (Section 2). For the comparison, which we can use to infer EDA parameters, we use Approximate Bayesian Computation (hereafter ABC; Diggle & Gratton 1984; Tavare et al. 1997; Pritchard et al. 1999; Beaumont et al. 2009; Del Moral et al. 2012). ABC is a simulation-based (or "likelihood-free") parameter inference framework that approximates the posterior probability distribution, $p(\theta \,|\, \mathrm{data})$, without requiring evaluations of the likelihood. Instead, ABC only requires a forward model of the observed data, a

prior that can be sampled, and a distance metric that quantifies the "closeness" to the observed data. Since ABC does not require evaluating the likelihood, it does not assume any functional form of the likelihood, which can significantly bias the inferred posterior (*e.g.* Hahn et al. 2019b). It also enables us to estimate the posterior using observables with difficult or intractable likelihoods (Hahn et al. 2017a)

In the simplest version of ABC, with a rejection sample framework (Pritchard et al. 1999), a proposal set of parameter values are drawn from the prior. The forward model is run with the proposal parameter values. The output of the forward model is then compared to the observed data using the distance metric. If the distance is within some small distance threshold, we keep the proposed parameters; otherwise, we discard them. Proposals are drawn until enough of them pass the threshold to sample the posterior. A rejection sampling framework requires a large number of evaluations of the forward model, which can be computationally costly. Many variations of ABC with more efficient sampling strategies have now been applied to astronomy and cosmology (*e.g.* Cameron & Pettitt 2012; Weyant et al. 2013; Ishida et al. 2015; Lin et al. 2016; Alsing et al. 2018). Among these methods, we use ABC in conjuction with Population Monte Carlo (PMC) importance sampling (Hahn et al. 2017a,b, 2019a).

The forward model in our scenario starts with the galaxies from our hydrodynamic simulations. We construct SEDs using their SFH and ZH, apply dust attenuation with the EDA model, and calculate the observables from the attenuated SED. For each simulation and a set of EDA parameters, our forward model produces G, R, NUV, and FUV absolute magnitudes. We use uninformative uniform priors on each of the EDA parameters and choose ranges to encompass constraints in the literature. The prior ranges of $m_{\tau,M_*}, m_{\tau,\mathrm{SSFR}}, c_\tau$ are chosen to conservatively include the A_V range and M_* and SFR dependence of Narayanan et al. (2018) and Salim & Narayanan (2020). Meanwhile, the prior ranges of $m_{\delta,M_*}, m_{\delta,\mathrm{SFR}}, c_\delta$ are chosen to conservatively include the δ range and M_* and SFR dependence of Leja et al. (2017) and Salim et al. (2018). We list the range of the priors in Table 1. We note that uniform priors on the EDA parameters do not necessarily produce uniform priors on τ_V or δ (*e.g.* Handley & Millea 2019). However, we are interested in marginalizing over dust attenuation and understanding the dependence of dust attenuation on galaxy properties, so we use uniformative priors on the EDA parameters and not on τ_V or δ.

ABC also requires a distance metric that quantifies the "closeness" of the forward model output to the observed data. For our distance metric, we use the L2 norm between the summary statistics, X, of the SDSS observation and our forward model:

$$\rho(\theta_{\mathrm{EDA}}) = \left[X^{\mathrm{SDSS}} - X^{\mathrm{FM}}(\theta_{\mathrm{EDA}})\right]^2. \tag{8}$$

θ_{EDA} are the EDA parameters. The summary statistics are based on the optical and UV color-magnitude relations, $(g-r) - R$ and $(FUV-NUV) - R$, of galaxies brighter than $M_r < -20$, the completeness limit of our SDSS sample (Figure 2). More specifically, for X, we calculate the number density in 3D bins of $g-r$, $FUV-NUV$, and M_r with widths 0.0625, 0.25, and 0.5 mags. We choose this summary statistic to fully exploit the observable-space predicted by the forward model. Later in Section 5 we discuss other potential observables.
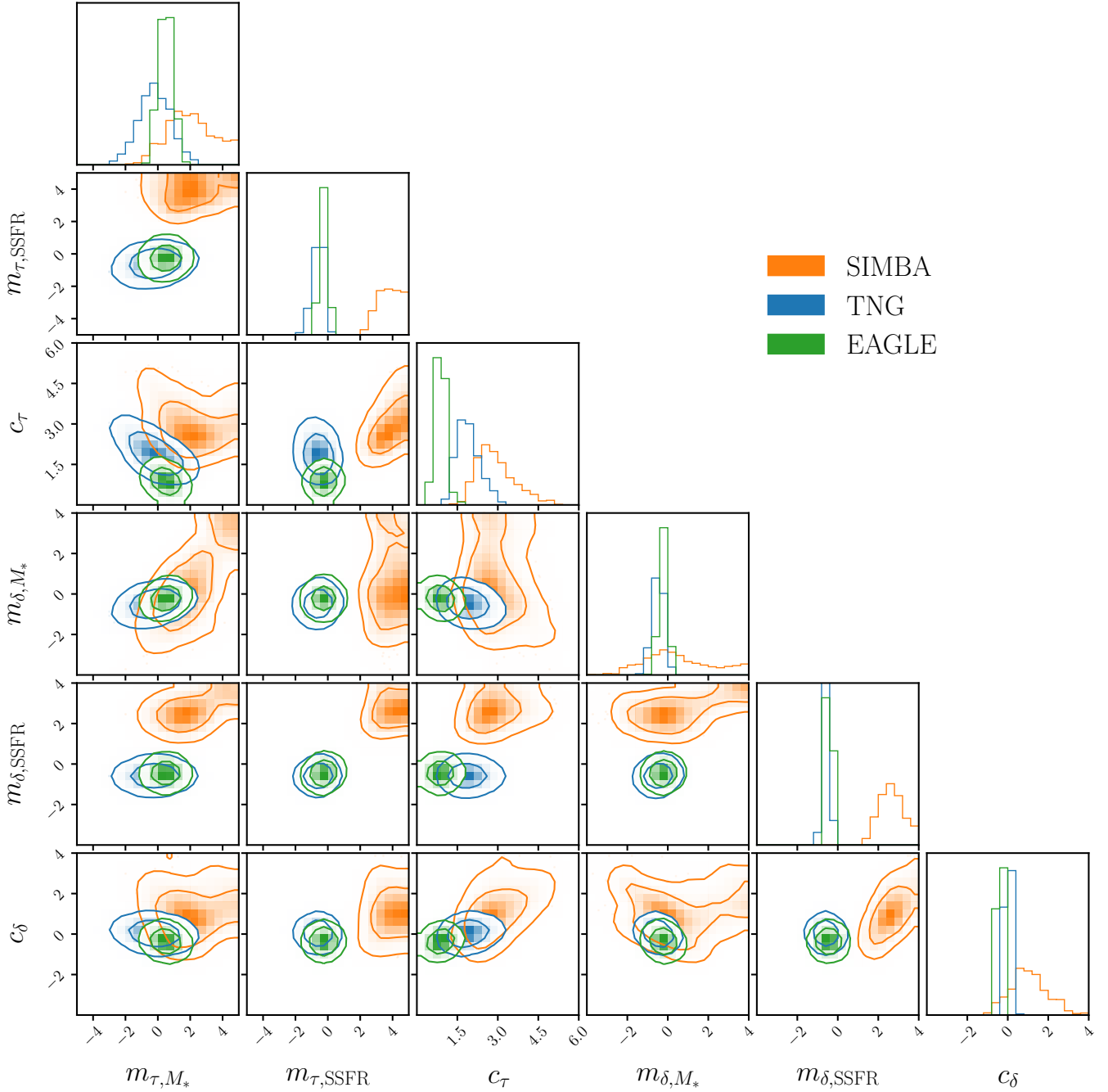
Figure 4. Posterior distributions of the EDA parameters for the SIMBA (orange), TNG (blue), and EA-GLE (green) hydrodynamical simulations. The contours mark the 68% and 95% confidence intervals. The posteriors are derived using the simulation-based inference method: Approximate Bayesian Computation with Population Monte Carlo (Section 4). We focus on the EDA posteriors for TNG and EAGLE since the EDA struggles to reproduce SDSS observations with SIMBA, which predicts an overabundance of starburst galaxies. Based on the posteriors, we find that *galaxies with higher M_* have overall higher dust attenuation and galaxies with higher SSFR have steeper attenuation curves.*
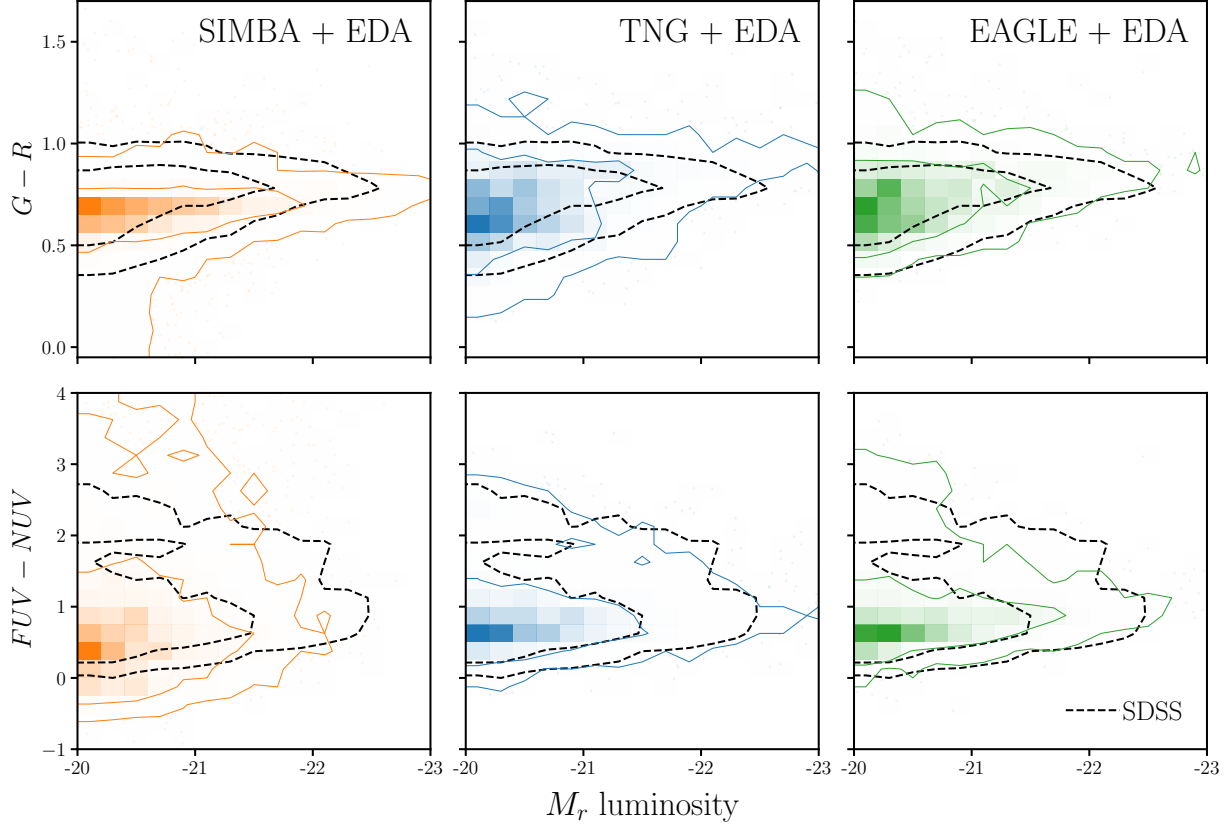
Figure 5. The optical and UV color-magnitude relations predicted by the DEM with the median ABC posteriors for the SIMBA (orange), TNG (blue), and EAGLE (green) hydrodynamical simulations. For comparison, we include the $(g-r)-M_r$ (top panels) and $(FUV-NUV)-M_r$ (bottom panels) relations for SDSS (black dashed). With the DEM, the simulations produce dramatically different observables than without any dust prescription (Figure 2). Hence, dust must be account for when interpreting and comparing simulations. Moreover, with the DEMs, all three simulations produce color-magnitude relations consistent with SDSS. Since different simulations can produce reproduce observations by varying dust, dust significantly limits our ability to constrain the physical processes that go into galaxy simulations.

ABC-PMC begins with an arbitrarily large threshold ϵ_1 and N proposals $\bar{\theta}_1$ sampled from the prior distribution. Each proposal is assigned a weight $w_1^i = 1/N$. Then for subsequent iterations $(i > 1)$, the threshold, ϵ_i, is set to the median distance of the previous iteration's proposals. New proposals are drawn from the previous iteration's proposals perturbed by a kernel and kept if their distance is blelow ϵ_i. This is repeated until we assemble a new set of N proposals $\bar{\theta}_i$. The entire process is repeated for the next iteration until convergence is confirmed. We use the Python implementation of Akeret et al. (2015)[6]. For further details on the ABC-PMC implementation, we refer readers to Hahn et al. (2017b) and Hahn et al. (2019a). In Figure 4, we present the posterior distributions of the EDA parameters derived from ABC-PMC for the SIMBA (orange), TNG (blue), and EAGLE (green) hydrodynamical simulations. The contours mark the 68% and 95% confidence intervals.

[6] https://abcpmc.readthedocs.io/en/latest/index.html

5. RESULTS

Without dust attenuation, all of the hydrodynamical simulations struggle to reproduce the $(g-r)-M_r$ and $(FUV-NUV)-M_r$ relations of SDSS (Figure 2). In optical, the simulations predict significantly bluer colors and find broader differences in color, ~0.5 mag, between star-forming and quiescent galaxies. In the UV, they predict quiescent galaxies with SSFR $< 10^{-12}yr^{-1}$ that have redder $FUV-NUV$ colors beyond SDSS observations. Meanwhile, for the rest of the galaxies, the simulations predict significantly bluer UV colors than SDSS.

With the EDA model, all of the simulations are able to reproduce the color-magnitude relations of SDSS. In Figure 5, we present the optical and UV color-magnitude relations predicted by the EDA for the SIMBA (orange), TNG (blue), and EAGLE (green) simulations. For the EDA parameters, we use the median of the posterior distributions inferred using ABC (Figure 4). The contours mark the 68% and 95% confidence intervals of the distributions.

Dust dramatically impacts the observables of simulations. The EDA affects the the optical and UV color-magnitude relations in three major ways to produce good agreement with SDSS. First, the EDA significantly reddens simulated galaxies in both the optical and UV. Overall, $g-r$ colors are ~0.25 mag redder and $FUV-NUV$ colors ~0.5 mag redder. Second, the EDA significantly attenuates (~0.5 mag) intrinsically blue galaxies (*i.e.* star-forming galaxies with log SSFR > -10.5). As a result, there are no longer luminous optically blue galaxies ($M_r < -21$ and $g-r < 0.5$) — consistent with observations. Lastly, in the UV, the EDA attenuates low SSFR quiescent galaxies that are intrinsically red in the UV ($FUV-NUV\sim3$ mag) by ~1 mag. Thus, unlike in Figure 2, the UV color-magnitude relations from the EDA do not have galaxies with high $FUV-NUV$ as in SDSS.

For SIMBA, the EDA substantially improves the agreement with observations; however, there are still some significant discrepancies in the color-magnitude relations with SDSS. The EDA products a $g-r$ color distribution that is too narrow and a $FUV-NUV$ distribution that is too wide. Also, the inferred EDA parameters for SIMBA differ significantly from the parameters of TNG and EAGLE (Figure 4). These discrepancies are primarily driven by the large population of high log SSFR > -9.5 "starburst" galaxies that lie above the SFS, which are *only* present in SIMBA (Figure 1). Without dust attenuation, these starburst galaxies are blue $g-r \sim 0.1$ and have high luminosity, $M_r < -22$. Such high luminosity blue galaxies are not present in observations, so these SIMBA galaxies need to be both strongly attenuated and reddened. This would, however, contradict the attenuation-slope relation established in both observations and simulations where galaxies with higher attenuation have shallower slopes (Inoue 2005; Chevallard et al. 2013; Salim et al. 2018; Salim & Narayanan 2020; Trayford et al. 2020). To further examine the impact of the starburst galaxies in SIMBA, we ran the EDA for SIMBA excluding galaxies with log SSFR > -9.5 and with median parameter values of the TNG and EAGLE posteriors. Without its starburst galaxies, SIMBA produces color-magnitude relations in good agreement with observations. *We conclude that the excess starburst population in SIMBA is in tension with observations.* Examining the prescriptions that produce the starburst in SIMBA is beyond the scope of this paper. Therefore, for the rest of the paper, we focus on the TNG and EAGLE simulations.

Figure 6. The attenuation-slope relation of the attenuation curves predicted by the EDA model for median posterior parameter values of TNG (blue) and EAGLE (green) simulations. We use A_V and $S = A(3000A)/A_V$ for attenuation and slope, respectively. For comparison, we include the observed attenuation-slope relation from GSWLC2 (Salim & Narayanan 2020). We also include the Milky Way (star) and mark the slope of the Calzetti (2001) curve (dashed). We derived the posteriors of the EDA model from comparing the UV and optical color-magnitude relation and do not fit any observed dust attenuation measurements. Yet, using a forward modeling approach, *we find excellent agreement between the attenuation-slope relation predicted by the EDA and observations.*

Previous works in the literature have also compared simulations with different dust prescriptions to observations in color-magnitude space. For EAGLE, Trayford et al. (2015) calculate colors and luminosities with the GALAXEV population synthesis models and a two-component screen model for dust. More recently, Trayford et al. (2017) calculated optical colors for EAGLE using SKIRT, a Monte Carlo radiative transfer code (Camps & Baes 2015), to model the dust. At stellar masses and luminosities comparable to our SDSS sample, both Trayford et al. (2015) and Trayford et al. (2017) produce red sequences bluer than in GAMA observations. Also, Trayford et al. (2015) predict an excess of luminous blue galaxies. Although a detailed comparison is difficult since both works compare to different observations, we note that with the EDA, EAGLE is able to successfully reproduce the position of the SDSS red sequence and does not predict a significant excess of luminous blue galaxies. Also using EAGLE and SKIRT, Baes et al. (2019) find that they overesimtate the observed cosmic SED (CSED) in the UV regime and produce significantly higher $FUV-NUV$ color than GAMA. The EDA predicts $FUV-NUV$ in good agreement with SDSS. For TNG, Nelson et al. (2018) calculate optical colors using a dust model that includes attenuation due to dense gas birth clouds surrounding young stellar populations and also due to simulated distribution of neutral gas and metals. They find bluer red sequence peaks and a narrower blue cloud compared to SDSS. We find neither of these discrepancies for the TNG with the EDA. The EDA is a simpler prescription for applying dust attenuation than the dust models in these works. Yet, with its flexibility, we are able to produce optical and UV color-magnitude relations that are in good agreement with observations. Furthermore, with its low computation costs we were able o fully explore our dust parameters.

5.1. *Reproducing Dust Observations*

We demonstrated above that we can use the EDA model in a forward model to accurately reproduce the observed color-magnitude relations. The EDA assigns dust attenuation curves to each simulated galaxy. This means that we can compare the dust attenuation assigned to the simulated galaxies to the dust attenuation measured from observed galaxies. In Figure 6, we present the attenuation-slope relation of the dust attenuation curves predicted by the EDA for the median posterior parameter values of TNG (blue) and EAGLE (green) simulations. For attenuation we use A_V and for slope we use the UV-optical slope, $S = A(3000A)/A_V$, commonly found in the literature. For comparison, we include the observed attenuation-slope relations of GSWLC2 galaxies (grey; Salim & Narayanan 2020), the Milky Way (star), and mark the slope of the Calzetti (2001) curve (dashed).

The attenuation-slope relation predicted by the EDA is in excellent agreement with observations. In both the EDA and observations, galaxies with higher attenuation have shallower slopes. We note that the difference in the A_V range is due to the stellar mass completeness limt of our sample, $M_* \gtrsim 10^{10} M_\odot$. Salim & Narayanan (2020) GSWLC2 sample extends down to $M_* \sim 10^{8.5} M_\odot$. The attenuation-slope relation is a consequence of the fact that dust scattering dominates absoprtion at low attenuation while dust absorption dominates at high attenuation (Gordon et al. 1994; Witt & Gordon 2000; Draine 2003; Chevallard et al. 2013). With the EDA, we are able to reproduce this physical relation solely from comparing the UV and optical color-magnitude relations. This not only demonstrates the robustness of the EDA, but it also highlights the advantages of our forward modeling approach.

We can more closely compare the attenuation curves predicted by the EDA to observations. In the left panels of Figure 7, we present the attenuation curves of star-forming galaxies predicted by the EDA model for the median posterior parameter values of TNG (blue) and EAGLE (green). In the top panel, we present galaxies with $M_* < 10^{11} M_\odot$; in the bottom we present galaxies with $M_* > 10^{11} M_\odot$. We define galaxies with $\log \text{SSFR} > -11$ as star-forming. The attenuation curves are normalized at $3000A$ and we present the variation in the attenuation curves in the shaded region, 1σ standard deviation about the median. For comparison, we include $A(\lambda)/A(3000A)$ from observations: Calzetti et al. (2000), Battisti et al. (2017), and Salim et al. (2018). We also include $A(\lambda)/A(3000A)$ measured from the Narayanan et al. (2018) simulation. The left panels of Figure 8 are the same as in Figure 7, except with attenuation curves that are not normalized. The normalized attenuation curves in Figure 7 emphasize the slope while the curves in Figure 8 emphasize the amplitude.

Based on the EDA, star-forming galaxies have higher dust attenuation at lower wavelengths. This is driven by both TNG and EAGLE predicting star-forming galaxies that are bluer than observations in the optical and UV wavelengths (Figure 2). As a result, the EDA significantly redden star-forming galaxies. This is also why TNG, which predicts an overall bluer star-forming population, has higher attenuation. In Figure 8, we also find that more massive star-forming galaxies have higher attenuation. This is because the simulations overpredict luminous blue star-forming galaxies, which must be attenuated to reproduce observations.

The EDA attenuation curves for both TNG and EAGLE are in good agreement with the observed Salim et al. (2018) attenuation curves. They are also consistent with the median curve of Narayanan et al. (2018). We ignore the discrepancies between the EDA and Narayanan et al. (2018) attenuation curves in the amplitude of UV dust bump, since we do not vary the UV bump in the EDA. The EDA attenuation curves are noticeably steeper than the Calzetti et al. (2000) and Battisti et al. (2017) curves. These attenuation curves, however, are derived from $M_* < 10^{9.9} M_\odot$ star-forming galaxies — below our M_* range. Overall, the EDA predicts attenuation curves that are in good agreement with both observations and radiative transfer simulations for star-forming galaxies. Again, the fact that we reproduce the detailed dust attenuation curves of star-forming galaxies in observations and simulations with the EDAwithout fitting for them, highlights the advantages of a forward modeling approach.
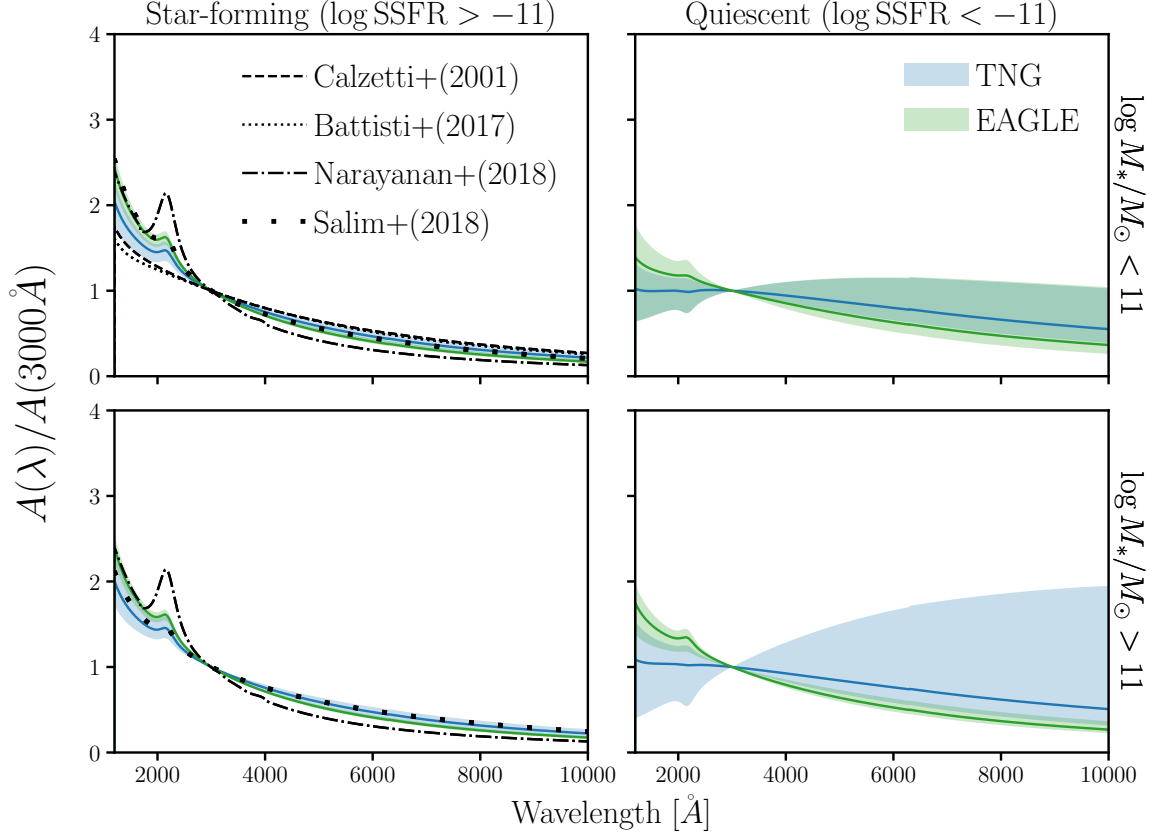
Figure 7. Attenuation curves predicted by the EDA for median posterior parameter values of the TNG (blue) and EAGLE (green) simulations. In the left and right panels, we present star-forming and quiescent galaxies classified using a $\log \mathrm{SSFR} = -11$ cut. In the top and bottom panels, we present galaxies with $M_* < 10^{11} M_\odot$ and $M_* > 10^{11} M_\odot$, respectively. The attenuation curves are normalized at $3000 \mathring{A}$ and we mark the 1σ standard deviation of the attenuation curves with the shaded region. For comparison, we include $A(\lambda)/A(3000 \mathring{A})$ measurements from observations (Calzetti et al. 2000; Battisti et al. 2017; Salim et al. 2018) and simulations (Narayanan et al. 2018). For star-forming galaxies, the Calzetti et al. (2000) and Battisti et al. (2017) attenuation curves are shallower than the EDA attenuation curves, but they probe less massive galaxies than our sample. For Salim et al. (2018), which probe a similar M_* range, we find goood agreement. We also find good agreement with median attenuation curve of star-forming galaxies in the radiative transfer simulations of Narayanan et al. (2018). With EDA, we can also constrain the attenuation curves of quiescent galaxies, which are challenging to directly measure in observations. Quiescent galaxies have significantly shallower attenuation curves than star-forming galaxies.

Figure 8. Same as Figure 7 except the attenuation curves are not normalized at $3000 \mathring{A}$. Based on the EDA, quiescent galaxies have significant UV and optical dust attenuation. However, they have significantly lower attenuation in the UV compared to star-forming galaxies and have shallow attenuation curves overall.

5.2. *The Attenuation Curves of Quiescent Galaxies*

We have demonstrated so far that the EDA is able reproduce the observed UV and optical color-magnitude relations and also predict dust attenuation curves of star-forming galaxies consistent with observations and radiative transfer simulations. In addition, the EDA also predicts dust attenuation curves of quiescent galaxies. This is particularly valuable since there are many challenges to measuring attenuation curves for quiescent galaxies directly from observations. Methods that rely on IR luminosities can be contaminated by MIR emission from AGN heating nearby dust (Kirkpatrick et al. 2015). Even SED fitting methods require accounting for AGN MIR emission (Salim et al. 2016; Leja et al. 2018; Salim et al. 2018). They also struggle to tightly constrain dust attenuation for quiescent galaxies since they are limited by the degeneracies with star formation history and metallicity.

With a forward modeling approach, we circumvent these challenges. We derive the attenuation curves necessary for quiescent galaxy population in simulations to reproduce the observed optical and UV photometry. In right panels of Figure 7, we present the attenuation curves of quiescent galaxies predicted by the EDA model for the median posterior parameter values of TNG (blue) and EAGLE (green). In the top and bottom panels, we present galaxies with $M_* < 10^{11} M_\odot$ and $M_* > 10^{11} M_\odot$, respectively. We define galaxies with $\log \mathrm{SSFR} < -11$ as quiescent. The right panels of Figure 8 are the same as in Figure 7, except the attenuation curves are not normalized.

For both TNG and EAGLE posteriors, the EDA predicts significant dust attenuation in quiescent galaxies. Compared to star-forming galaxies, however, they have lower attenuation in the UV and much shallower attenuation curves. The amplitude of the attenuation is driven by the fact that both TNG and EAGLE — without dust — predict quiescent galaxies that are too luminous compared to observations. Hence, significant attenuation is necessary to lower their luminosity. Meanwhile, the shallow slope is driven by the simulations predicting quiescent galaxies that are bluer in the optical but redder in the UV than observations. The EDA optically reddens the quiescent galaxies but maintains a shallow enough slope to reproduce the UV color-magnitude relation. This is also why TNG has a shallower slope than EAGLE: TNG has an optically redder quiescent population and more quiescent galaxies with high $FUV-NUV$ color.

Given the challenges in observationally measuring attenuation curves of quiescent galaxies, the predictions of the bestfit EDA models for TNG and EAGLE again highlight the advantages of a forward modeling approach and provide valuable insights into dust attenuation in quiescent galaxies. *Quiescent galaxies have significant UV and optical attenuation with shallow slopes.*

5.3. *The Galaxy – Dust Connection*

Since the EDA models predict dust attenuation for all galaxies in the sample, they allow us to shed light on the connection between galaxy properties and dust attenuation. More specifically, the EDA parameters constraints (Figure 4) and the predicted attenuation curves (Figures 7 and 8) reveal the stellar mass and SSFR dependence of dust attenuation. Focusing first on the M_* dependence, we find that TNG has little M_* dependence in τ_V ($m_{\tau,M_*} = -0.15^{+0.83}_{-0.91}$) while EAGLE has a significant M_* dependence ($m_{\tau,M_*} = 0.55^{+0.40}_{-0.37}$). Meanwhile, we find significant M_* dependence in δ for both TNG ($m_{\delta,M_*} = -0.44^{+0.27}_{-0.26}$) and EAGLE ($m_{\delta,M_*} = -0.20^{+0.17}_{-0.17}$) — *i.e.* more massive galaxies have

steeper slopes (Figure 4). The M_* dependence in τ_V and δ are further illustrated in the attenuation curves in Figure 8. For TNG, there is little difference in the V-band attenuation between the top and bottom panels. However, more massive galaxies have steeper slopes with similar A_V so they have significantly higher UV attenuation. For EAGLE, more massive galaxies have both higher V-band and UV attenuation. Overall, we find that more massive galaxies have higher attenuation, which is consistent with the literature. Burgarella et al. (2005), for instance, found significant positive M_* dependence in FUV attenuation in NUV-selected and FIR-selected samples. Garn & Best (2010) and Battisti et al. (2016) also find higher attenuation in more massive SDSS star-forming galaxies. Most recently, Salim et al. (2018) find higher V and FUV attenuation for more masssive star-forming galaxies in GSWLC2.

Next, we examine the SSFR dependence of dust attenuation. For both TNG and EAGLE, we find a significantly negative SSFR dependence in τ_V ($m_{\tau,\mathrm{SSFR}} = -0.56^{+0.36}_{-0.30}$ and $-0.24^{+0.21}_{-0.20}$, respectively) as well as δ ($m_{\delta,\mathrm{SFR}} = -0.57^{+0.14}_{-0.112}$ and $-0.43^{+0.10}_{-0.09}$, respectively). In other words, galaxies with higher SSFR have lower V-band attenuation and steeper attenuation curves. From the attenuation curves in Figure 8, we similarly find that star-forming galaxies have attenuation curves with slightly lower A_V but substantially higher UV attenuation. Quiescent galaxies, on the other hand, have significantly shallower attenuation curves. Although observations have examined the SSFR dependence of dust attenuation, they cannot be compared our findings since they focus only on star-forming galaxies, due to the difficulty in observationally constraining the attenuation curve in quiescent galaxies (*e.g.* Garn & Best 2010; Reddy et al. 2015; Battisti et al. 2016, 2017; Salim et al. 2018). In summary, from the bestfit EDA models of TNG and EAGLE, we find that *galaxies with higher M_* have overall higher dust attenuation and galaxies with higher SSFR have steeper attenuation curves.*

5.4. *Discussion*

We make a number of assumptions and choices in the EDA. For instance, EDA assigns A_V using the slab model (Eq. 3). We use the slab model because it reproduces the correlation between attenuation and inclination in observations (Conroy 2010; Wild et al. 2011; Battisti et al. 2017; Salim & Narayanan 2020) and simulations (*e.g.* Chevallard et al. 2013; Narayanan et al. 2018; Trayford et al. 2020). It also reproduces the SDSS A_V distribution (Figure 10). If we replace the slab model with a more flexible model for sampling A_V using truncated normal distributions, we find that our results are not significantly impacted (see Appendix B for details). Therefore, we conclude that our results do not sigficantly depend on our choice of the slab model.

Besides the slab model, we use a simple parameterization of τ_V and δ in the EDA. Both τ_V and δ depend linearly on $\log M_*$ and $\log \mathrm{SSFR}$. This linear parameterization was choice for soley for its simplicity—the EDA can easily be extended to more flexible parameterizations. In fact, a more flexible parameterization would likely reduce some of the discrepancies with the SDSS color-magnitude relations. The EDA produces broader distributions of optical colors than SDSS. Few galaxies in SDSS have $g-r > 1$. while some galaxies in the EDA broadly extend beyond this cut-off. In the UV, the EDA struggles to accurately reproduce the redder portions ($FUV-NUV > 1.5$) of the UV color-magnitude relation. The main challenges for a more flexible parameterization would be

Figure 9. IR dust emission luminosity predicted by the EDA with median parameter values of the TNG (blue) and EAGLE (green) posteriors as a function of M_r. The dust emission is estimated assuming the da Cunha et al. (2008) energy balance. Despite reproducing the same SDSS UV and optical color-magnitude relations, *the bestfit EDA models for TNG and EAGLE predict significantly different IR dust emission*. Therefore, including IR observations will significantly improve the constraints on EDA parameters and allow us to better differentiate galaxy formation models.

model selection and finding a well-motivated parameterization. Nevertheless, for SDSS observations, the EDA using parameter values from the TNG and EAGLE posteriors find good agreement.

The fact that we can use the EDA to reproduce SDSS observations for different hydrodynamical simulations highlight two key points. First, it demonstrates that accounting for dust attenuation is essential when comparing simulations to observations. None of the simulations reproduce the UV and optical color-magnitude relation without dust attenuation (Figure 2). Second, it also highlights the limitations in our current understanding of dust. The EDA is built on our current understanding of dust attenuation in galaxies: *e.g.* the Noll et al. 2009 parameterization, the UV bump, the slab model, etc. Yet with the EDA, two simulations that predict galaxy populations with significantly different physical properties (Figure 1) can reproduce the same SDSS observations. This suggests that dust is highly degenerate with the differences between simulations. Put another way — if we were to marginalize over dust in our comparison to observations, we would not be able to differentiate between the different galaxy physics prescriptions in the simulations. Hence, current limitations in our understanding of dust is a major bottleneck for investigating galaxy formation using simulations.

Fortunately, there are many avenues for improving our understanding of dust with a forward modeling approach. In this work, we used a restrictive $M_r < -20$ complete SDSS galaxy sample. Instead of imposing a completeness limit, we can include the actual SDSS selection function in the forward model (*e.g.* Dickey et al. 2020). This would allow us to compare the simulations with EDA to a substantially larger galaxy sample. Upcoming surveys, such as the Bright Galaxy Survey (BGS) of the Dark Energy Spectroscopic Instrument (DESI; DESI~Collaboration et al. 2016; Ruiz-Macias et al. 2020) and galaxy evolution survey of the Prime Focus Spectrograph (PFS; Takada et al. 2014; Tamura et al. 2016), will also vastly expand galaxy observations. BGS, for instance, will measure $10\times$ the number of galaxy spectra as SDSS out to $z \sim 0.4$. A larger more statistically powerful observation sample will allow us to place tighter constraints on EDA parameters and enable an actual comparison of the underlying simulations.

In this work, we also only used observables derived from UV and optical photometry. We only examine one side of the impact that dust has on galaxy spectra. While dust attenuates light in the optical and UV, it emits light in IR. In fact, even though the TNG and EAGLE simulations reproduce the same UV and optical color-magnitude relations with the EDA, they predict significnatly different dust emission in the IR. In Figure 9, we present IR dust emission luminosity, $L_{\rm IR}$, predicted by the EDA with median parameter values of the TN (blue) and EAGLE (green) posteriors as as a function of the r-band absolute magnitude, M_r. The dust emissions are estimated using the standard energy

balance assumption — *i.e.* all starlight attenuated by dust is reemitted in the IR (da Cunha et al. 2008).

Despite reproducing the same SDSS UV and optical color-magnitude relations, the bestfit EDA models for TNG and EAGLE predict significantly different IR dust emission. The bestfit EDA model for TNG predicts an overall $\sim$0.3 dex ($2\times$) higher dust emissions than for EAGLE. Higher dust emission for TNG is consistent with the higher c_τ we infer for TNG (Figure 4). It is also consistent with the fact that TNG predicts bluer galaxies and more luminous quiescent galaxies with red $FUV-NUV$ color than EAGLE (Figure 2). Since IR dust emission measures the total dust attenuation, IR observations would specifically constrain the EDA and therefore break degeneracies between dust and the galaxy physics in simulations. A number of upcoming observations will probe the IR (*e.g.* @tjitske observations you mentioned). BGS galaxies will also have IR photometry from NEOWISE (Meisner et al. 2018). TODO

6. SUMMARY

In this work, we present the EDA, a framework for statistically applying dust attenuation to simulated galaxy populations. It uses a parameterization of the attenuation curves motivated from observations (Noll et al. 2009) and a flexible method for sampling the attenuation curve parameters that includes correlations with galaxy properties (M_* and SSFR). We apply the EDA to three state-of-the-art hydrodynamical simulations (SIMBA, TNG, and EAGLE) and forward model the optical and UV color-magnitude relations. We then compare the forward modeled simulations to a $M_r < -20$ complete SDSS galaxy sample using simulation-based inference. Based on this comparison, we find the following results:

- Dust attenuation is essential for simulations to reproduce observations. Without dust attenuation, all of the hydrodynamical simulations struggle to reproduce the observed UV and optical color-magnitude relation.

- With the EDA, the TNG and EAGLE simulations are able to produce UV and optical color-magnitude relations in good agreement with SDSS observations. SIMBA, however, overpredicts a substantial starburst galaxy population and in order to reproduce observations, these galaxies require both high attenuation and reddening, which goes against the observed attenuation-slope relation.

- The attenuation curves predicted by the bestfit EDA for TNG and EAGLE are in excellent agreement with the observed attenuation-slope relation. They also closely reproduce the observed attenuation curves of star-forming galaxies. The success of the EDA in reproducing these observations, which were not included in the comparison, highlights the advantages of a forward modeling approach.

- Lastly, the EDA sheds light on dust attenuation in quiescent galaxies, which remains poorly understood due to observations challenges. We find that quiescent galaixes have significant UV and optical attenuation with shallow attenuation curves. For all galaxies, we find that more

massive galaxies have higher overall dust attenuation while galaxies with higher SSFR have steeper attenuation curves.

Our results clearly demonstrate that the EDA and a forward modeling approach provides key insights into dust attenuation. For those uninterested in dust, the EDA also provides a framework for marginalizing over dust when comparing simulations to observations. In the case of SIMBA, we found that dust attenuation is insufficient to accurately reproduce observations due to its starburst population. For TNG and EAGLE, however, dust attenuation is highly degenerate with differences in their galaxy physics prescriptions. Even though TNG and EAGLE predict galaxy populations with significantly different physical properties, there is enough uncertainty in our understanding of dust that by adjusting attenuation alone both TNG and EAGLE can reproduce the same SDSS observations. This also suggests that any comparisons across simulations must marginalize over dust attenuation or run the risk of overinterpretation. Therefore, our current understanding of dust, or lack of, limit our ability to distinguish between the various hydrodynamical models and is a major bottleneck for investigating galaxy formation using simulations.

The forward modeling approach we present offers many avenues for improving on our understanding of dust. In this paper, we used a relatively restrictive M_r complete SDSS galaxy sample. Comparison to a larger observed galaxy sample will place tighter constraints on EDA parameters and enable better differentiation between the simulations. One way to expand the observed galaxy sample would be to remove the M_r completeness limit by including the selection function to our forward model. Upcoming surveys, such as the DESI Bright Galaxy Survey and the PFS Galaxy Evolution Survey, will also soon provide much larger galaxy samples. Furthermore, IR observations, which measure dust emission and trace dust attenuation, also have the potential to tightly constrain the EDA parameters and therefore break degeneracies between dust and the galaxy physics in simulations. In future works, we will apply the EDA and a forward mdoeling approach to more statistically powerful samples and include IR observables in order to tightly constrain and reveal new insights into dust attenuation.

APPENDIX

A. RESOLUTION EFFECTS

Figure demonstrating imprint SFR=0 leave on the observable space and how we deal with them so we can ignore them...

B. BEYOND THE SLAB DEM

A major assumption of our fiducial DEM is that we sample the amplitude of attenuation from the slab model. The slab model makes the simplifying assumption that dust in galaxies are in a slab-like geometry and illuminated by the stellar radiation source (Somerville & Primack 1999). Then, for a given τ_V, the attenuation depends solely on the orientation of the galaxy. This simplification, ignores any complexities in the star-to-dust geometry that impact the shape of the attenuation curve (Witt Gordon 1996, 2000, Seon Drain 2016).   TODO

Besides its simplifications, the slab model predicts A_V distribution with significant differences than the A_V distributions measured from observations. In Figure 10, we compare the A_V distribution predicted by the slab model (black) to the A_V distribution of star-forming galaxies in our SDSS sample (blue). The A_V values are derived using SED fitting from the Brinchmann et al. (2004) MPA-JHU catalog and how are the SF galaxies classified. The slab model A_V values are derived using Eq. 3 and 4 with M_*s and SFRs from the same SDSS sample and the inclinations, i, are uniformly sampled over the range $[0, \pi/2]$. With $\{m_{\tau,1}, m_{\tau,2}, c_\tau\}$ chosen to reproduce the observed A_V distribution, the slab model can reproduce the overall shape. However, it predicts an extended high A_V tail not found in observations.   TODO

Given these shortcomings of the slab model, we want to ensure that our results do not hinge on the slab model. Modeling the star-to-dust geometries with increased complexities, however, would involve expensive hydrodynamic simulations and dust radiative transfer calculations (*e.g.* Narayanan et al. 2018)jonsson2006, rocha2008, natale2015,hayward smith2015,hou2017,trayford2020. We instead take an empirical approach and implement a flexible model for sampling A_V based on a truncated normal distribution: TODO

$$A_V \sim \mathcal{N}_T(\mu_{A_V}, \sigma_{A_V}) = \frac{\mathcal{N}(\mu_{A_V}, \sigma_{A_V})}{1 - \Phi\left(-\frac{\mu_{A_V}}{\sigma_{A_V}}\right)}. \tag{B1}$$

Here, $\mathcal{N}$ is the standard normal distribution and $\Phi(x) = \frac{1}{2}\left(1 + \mathrm{erf}(x/\sqrt{2})\right)$ is the cumulative distribution function of $\mathcal{N}$. μ_{A_V} and σ_{A_V} are the mean and variance of the truncated normal distribution. Similar to Eq. 4, we allow μ_{A_V} and σ_{A_V} to depend on the physical properties of galaxies:

$$\mu_{A_V} = m_{\mu,1}(\log\ M_* - 10.) + m_{\mu,2}\log\ \mathrm{SFR} + c_\mu \tag{B2}$$

$$\sigma_{A_V} = m_{\sigma,1}(\log\ M_* - 10.) + m_{\sigma,2}\log\ \mathrm{SFR} + c_\sigma. \tag{B3}$$

The A_V distribution from our truncated normal (orange dashed) closely reproduces the observed SDSS A_V distribution (Figure 5). N_T is able to reproduce the overall skewness but unlike the slab model, it does not have a long high A_V tail. With more free parameters and a functional form that closely resembles the observed A_V distribution, the truncated normal model provides a flexible altnerative to the slab model and we include it in our analysis.

REFERENCES

Abazajian K. N., et al., 2009, The Astrophysical Journal Supplement Series, 182, 543

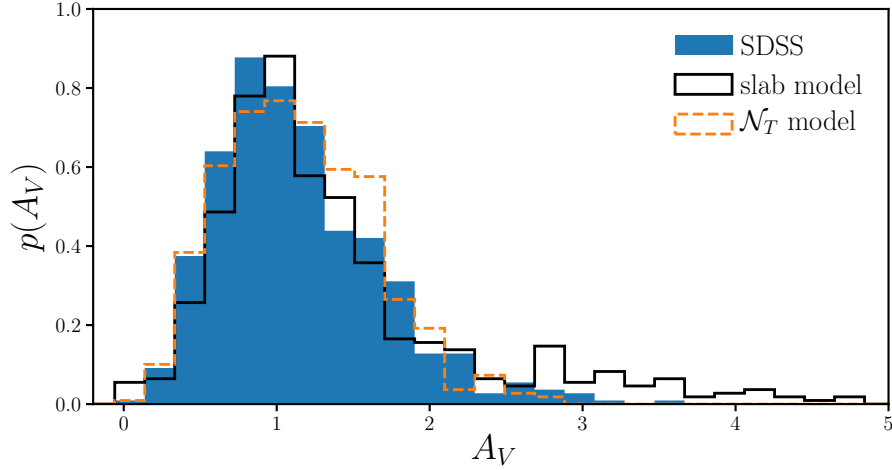Aihara H., et al., 2011, The Astrophysical Journal Supplement Series, 193, 29

Figure 10. Comparison of A_V distribution of SDSS star-forming galaxies (blue) to predictions from the slab model (Eq. 3; black). detail on how SDSS SF galaxies are classified. The slab model assumes that there's a slab of dust in front of a galaxy. We use $\tau_V = 2$ for the slab model above. Regardless of τ_V, however, the slab model predicts a significantly more asymmetric and peaked A_V distribution than observations. Given this disagreement, *we include in our analysis a DEM with an empirical prescription for A_V based on a truncated normal distribution, which better reproduce the observed A_V distribution* (Section B).

Akeret J., Refregier A., Amara A., Seehars S., Hasner C., 2015, Journal of Cosmology and Astroparticle Physics, 2015, 043

Alsing J., Wandelt B., Feeney S., 2018, arXiv:1801.01497 [astro-ph]

Anglés-Alcázar D., Davé R., Faucher-Giguère C.-A., Özel F., Hopkins P. F., 2017, Monthly Notices of the Royal Astronomical Society, 464, 2840

Baes M., Trčka A., Camps P., Nersesian A., Trayford J., Theuns T., Dobbels W., 2019, arXiv:1901.08878 [astro-ph]

Battisti A. J., Calzetti D., Chary R.-R., 2016, The Astrophysical Journal, 818, 13

Battisti A. J., Calzetti D., Chary R.-R., 2017, The Astrophysical Journal, 840, 109

Beaumont M. A., Cornuet J.-M., Marin J.-M., Robert C. P., 2009, Biometrika, 96, 983

Blanton M. R., Roweis S., 2007, The Astronomical Journal, 133, 734

Blanton M. R., et al., 2005, The Astronomical Journal, 129, 2562

Blanton M. R., Kazin E., Muna D., Weaver B. A., Price-Whelan A., 2011, The Astronomical Journal, 142, 31

Booth C. M., Schaye J., 2009, Monthly Notices of the Royal Astronomical Society, 398, 53

Brinchmann J., Charlot S., White S. D. M., Tremonti C., Kauffmann G., Heckman T., Brinkmann J., 2004, Monthly Notices of the Royal Astronomical Society, 351, 1151

Burgarella D., Buat V., Iglesias-Páramo J., 2005, Monthly Notices of the Royal Astronomical Society, 360, 1413

Calzetti D., 2001, New Astronomy Reviews, 45, 601

Calzetti D., Armus L., Bohlin R. C., Kinney A. L., Koornneef J., Storchi-Bergmann T., 2000, The Astrophysical Journal, 533, 682

Cameron E., Pettitt A. N., 2012, Monthly Notices of the Royal Astronomical Society, 425, 44

Camps P., Baes M., 2015, Astronomy and Computing, 9, 20

Chabrier G., 2003, Publications of the Astronomical Society of the Pacific, 115, 763

Chevallard J., Charlot S., Wandelt B., Wild V., 2013, Monthly Notices of the Royal Astronomical Society, 432, 2061

Conroy C., 2010, Monthly Notices of the Royal Astronomical Society, 404, 247

Conroy C., 2013, Annual Review of Astronomy and Astrophysics, 51, 393

Conroy C., Gunn J. E., White M., 2009, The Astrophysical Journal, 699, 486

Conroy C., White M., Gunn J. E., 2010, The Astrophysical Journal, 708, 58

Crain R. A., et al., 2015, Monthly Notices of the Royal Astronomical Society, 450, 1937

DESI~Collaboration et al., 2016, arXiv:1611.00036 [astro-ph]

Dalla Vecchia C., Schaye J., 2012, Monthly Notices of the Royal Astronomical Society, 426, 140

Davé R., Thompson R., Hopkins P. F., 2016, Monthly Notices of the Royal Astronomical Society, 462, 3265

Davé R., Rafieferantsoa M. H., Thompson R. J., 2017a, arXiv:1704.01135 [astro-ph]

Davé R., Rafieferantsoa M. H., Thompson R. J., Hopkins P. F., 2017b, Monthly Notices of the Royal Astronomical Society, 467, 115

Davé R., Anglés-Alcázar D., Narayanan D., Li Q., Rafieferantsoa M. H., Appleby S., 2019, Monthly Notices of the Royal Astronomical Society, 486, 2827

Del Moral P., Doucet A., Jasra A., 2012, Statistics and Computing, 22, 1009

Dickey C. M., et al., 2020, arXiv e-prints, 2010, arXiv:2010.01132

Diggle P. J., Gratton R. J., 1984, Journal of the Royal Statistical Society. Series B (Methodological), 46, 193

Draine B. T., 2003, The Astrophysical Journal, 598, 1017

Fontanot F., Somerville R. S., Silva L., Monaco P., Skibba R., 2009, Monthly Notices of the Royal Astronomical Society, 392, 553

Galliano F., Galametz M., Jones A. P., 2018, Annual Review of Astronomy and Astrophysics, 56, 673

Garn T., Best P. N., 2010, Monthly Notices of the Royal Astronomical Society, 409, 421

Genel S., et al., 2014, Monthly Notices of the Royal Astronomical Society, 445, 175

Gonzalez-Perez V., Lacey C. G., Baugh C. M., Frenk C. S., Wilkins S. M., 2013, Monthly Notices of the Royal Astronomical Society, 429, 1609

Gordon K. D., Witt A. N., Carruthers G. R., Christensen S. A., Dohne B. C., 1994, The Astrophysical Journal, 432, 641

Granato G. L., Lacey C. G., Silva L., Bressan A., Baugh C. M., Cole S., Frenk C. S., 2000, The Astrophysical Journal, 542, 710

Hahn C., Vakili M., Walsh K., Hearin A. P., Hogg D. W., Campbell D., 2017a, Monthly Notices of the Royal Astronomical Society, 469, 2791

Hahn C., Tinker J. L., Wetzel A. R., 2017b, The Astrophysical Journal, 841, 6

Hahn C., Tinker J. L., Wetzel A., 2019a, arXiv:1910.01644 [astro-ph]

Hahn C., Beutler F., Sinha M., Berlind A., Ho S., Hogg D. W., 2019b, Monthly Notices of the Royal Astronomical Society, 485, 2956

Hahn C., et al., 2019c, The Astrophysical Journal, 872, 160

Handley W., Millea M., 2019, Entropy, 21, 272

Hayward C. C., Smith D. J. B., 2015, Monthly Notices of the Royal Astronomical Society, 446, 1512

Hopkins P. F., 2015, Monthly Notices of the Royal Astronomical Society, 450, 53

Hopkins P. F., et al., 2017, arXiv:1707.07010 [astro-ph]

Hou K.-C., Hirashita H., Nagamine K., Aoyama S., Shimizu I., 2017, Monthly Notices of the Royal Astronomical Society, 469, 870

Inoue A. K., 2005, Monthly Notices of the Royal Astronomical Society, 359, 171

Ishida E. E. O., et al., 2015, Astronomy and Computing, 13, 1

Jonsson P., 2006, Monthly Notices of the Royal Astronomical Society, 372, 2

Kirkpatrick A., Pope A., Sajina A., Roebuck E., Yan L., Armus L., Díaz-Santos T., Stierwalt S., 2015, The Astrophysical Journal, 814, 9

Kriek M., Conroy C., 2013, The Astrophysical Journal Letters, 775, L16

Leja J., Johnson B. D., Conroy C., van Dokkum P. G., Byler N., 2017, The Astrophysical Journal, 837, 170

Leja J., Johnson B. D., Conroy C., van Dokkum P., 2018, The Astrophysical Journal, 854, 62

Lin C.-A., Kilbinger M., Pires S., 2016, Astronomy and Astrophysics, 593, A88

McAlpine S., et al., 2016, Astronomy and Computing, 15, 72

Meisner A. M., Lang D., Schlegel D. J., 2018, Research Notes of the American Astronomical Society, 2, 1

Narayanan D., Conroy C., Davé R., Johnson B. D., Popping G., 2018, The Astrophysical Journal, 869, 70

Natale G., Popescu C. C., Tuffs R. J., Debattista V. P., Fischera J., Grootes M. W., 2015, Monthly Notices of the Royal Astronomical Society, 449, 243

Nelson D., et al., 2015, Astronomy and Computing, 13, 12

Nelson D., et al., 2018, Monthly Notices of the Royal Astronomical Society, 475, 624

Noll S., Burgarella D., Giovannoli E., Buat V., Marcillac D., Muñoz-Mateos J. C., 2009, Astronomy and Astrophysics, 507, 1793

Pillepich A., et al., 2018, Monthly Notices of the Royal Astronomical Society, 473, 4077

Pritchard J. K., Seielstad M. T., Perez-Lezaun A., Feldman M. W., 1999, Molecular Biology and Evolution, 16, 1791

Reddy N. A., et al., 2015, The Astrophysical Journal, 806, 259

Rocha M., Jonsson P., Primack J. R., Cox T. J., 2008, Monthly Notices of the Royal Astronomical Society, 383, 1281

Ruiz-Macias O., et al., 2020, arXiv:2007.14950 [astro-ph]

Salim S., Narayanan D., 2020, arXiv:2001.03181 [astro-ph]

Salim S., et al., 2016, The Astrophysical Journal Supplement Series, 227, 2

Salim S., Boquien M., Lee J. C., 2018, The Astrophysical Journal, 859, 11

Salmon B., et al., 2016, The Astrophysical Journal, 827, 20

Schaye J., et al., 2015, Monthly Notices of the Royal Astronomical Society, 446, 521

Seon K.-I., Draine B. T., 2016, The Astrophysical Journal, 833, 201

Somerville R. S., Primack J. R., 1999, Monthly Notices of the Royal Astronomical Society, 310, 1087

Somerville R. S., Gilmore R. C., Primack J. R., Domínguez A., 2012, Monthly Notices of the Royal Astronomical Society, 423, 1992

Springel V., 2005, Monthly Notices of the Royal Astronomical Society, 364, 1105

Springel V., et al., 2018, Monthly Notices of the Royal Astronomical Society, 475, 676

Steinacker J., Baes M., Gordon K. D., 2013, Annual Review of Astronomy and Astrophysics, 51, 63

Takada M., et al., 2014, Publications of the Astronomical Society of Japan, 66, R1

Tamura N., et al., 2016, in Ground-Based and Airborne Instrumentation for Astronomy VI. eprint: arXiv:1608.01075, p. 99081M, doi:10.1117/12.2232103

Tavare S., Balding D. J., Griffiths R. C., Donnelly P., 1997, Genetics, 145, 505

Tinker J., Wetzel A., Conroy C., 2011, preprint, 1107, arXiv:1107.5046

Trayford J. W., et al., 2015, Monthly Notices of the Royal Astronomical Society, 452, 2879

Trayford J. W., et al., 2017, Monthly Notices of the Royal Astronomical Society, 470, 771

Trayford J. W., Lagos C. d. P., Robotham A. S. G., Obreschkow D., 2020, Monthly Notices of the Royal Astronomical Society, 491, 3937

Trčka A., et al., 2020, arXiv:2003.12576 [astro-ph]

Tress M., et al., 2018, Monthly Notices of the Royal Astronomical Society, 475, 2363

Vogelsberger M., et al., 2014, Monthly Notices of the Royal Astronomical Society, 444, 1518

Walcher J., Groves B., Budavári T., Dale D., 2011, Astrophysics and Space Science, 331, 1

Weinberger R., et al., 2018, Monthly Notices of the Royal Astronomical Society, 479, 4056

Weyant A., Schafer C., Wood-Vasey W. M., 2013, The Astrophysical Journal, 764, 116

Wild V., Charlot S., Brinchmann J., Heckman T., Vince O., Pacifici C., Chevallard J., 2011, Monthly Notices of the Royal Astronomical Society, 417, 1760

Wilkins S. M., Gonzalez-Perez V., Lacey C. G., Baugh C. M., 2012, Monthly Notices of the Royal Astronomical Society, 424, 1522

Witt A. N., Gordon K. D., 1996, The Astrophysical Journal, 463, 681

Witt A. N., Gordon K. D., 2000, The Astrophysical Journal, 528, 799

da Cunha E., Charlot S., Elbaz D., 2008, Monthly Notices of the Royal Astronomical Society, 388, 1595